

Analytic continuation of Green's functions with a neural network

Fakher Assaad , Johanna Erdmenger , Anika Götz, René Meyer , Martin Rackl* and Yanick Thurn[†] 

Institute for Theoretical Physics and Astrophysics and
Würzburg-Dresden Cluster of Excellence ct.qmat
Julius-Maximilians-Universität Würzburg
97074 Würzburg, Germany

* martin.rackl@uni-wuerzburg.de , † yanick.thurn@uni-wuerzburg.de

24th February 2026

Abstract

An important problem in many-body physics is to reconstruct the spectral density from the imaginary-time domain Green's function. Typically, the imaginary-time Green's function is generated by Monte Carlo methods. As the one-point fermionic kernel diverges exponentially for large frequencies, numerical noise generically causes instabilities. We use a convolutional neural network to obtain the spectral density for a given imaginary time Green's function. The network is trained by data which we generate using random Gaussians. We improve the training data set available by including collision centers for the Gaussians rather than employing uniformly distributed Gaussians. Our network is constructed in such a way that its output fulfills positive semi-definiteness. We compare the results of our network with results of the Maximum Entropy method (MaxEnt), a standard method for the same reconstruction problem for the spectral density. This comparison is performed for three different cases, namely our Gaussian based test data as well as two physical models, the 1d Hubbard model showing spin-charge separation, and the two-dimensional SSH model in the self-consistent Born approximation. We find that the network outperforms MaxEnt when presented data close to the training set. For the physical models considered, MaxEnt recognizes physical features more precisely as compared to our network prediction. While it is hard to improve MaxEnt, the quality of the network depends on the training data set which can be systematically enhanced and improved.

Contents

1	Introduction	2
2	Computational aspects	3
2.1	Generating the training data	4
2.2	Description of the training setup	4
2.2.1	Structure of the neural network	5
2.2.2	Loss function and trainer	5
3	Performance & physical results	6
3.1	Comparison to MaxEnt on validation data	6
3.2	Spin-Charge separation in 1D Hubbard model	9
3.3	The two-dimensional SSH model: self-consistent Born approximation	9
4	Conclusion and Outlook	12
	References	13

1 Introduction

Some problems in theoretical physics are easy to solve in one direction, but the inverse problem is hard, in particular it is prone to instabilities. One example is the relation between imaginary time domain Green's function and real frequency Green's function. Solving for the Green's function in the real frequency domain from euclidean domain lattice data is however one of the most important problems both in the fields of high energy and condensed matter physics, as many strongly interacting problems in these fields can only be solved by euclidean lattice simulations. Solving this analytic continuation problem is for example important for the determination of the transport coefficients, such as the shear viscosity [1–3], of the quark gluon plasma, or for understanding spectroscopic experiments such as neutron scattering, angle-resolved photoemission, or scanning tunneling microscopy in the realm of the solid state [4, 5]. This analytic continuation is a so-called ill-posed problem, as it is resistant to analytical solution and simple numerical approaches, and lacks essential properties such as uniqueness or stability of solutions [6]. The crucial aspect of this problem is the instability of calculating the real frequency domain spectral density function $A(\omega) = \frac{1}{\pi} \text{Im}(G^R(\omega))$ from the imaginary time domain Green's function $\mathcal{G}(\tau)$ via

$$\mathcal{G}(\tau) = - \int d\omega \frac{e^{-\omega\tau}}{1 + e^{-\frac{\hbar\omega}{k_B T}}} A(\omega) = - \int d\omega \mathcal{K}(\tau, \omega) A(\omega), \quad (1)$$

with $\mathcal{K}(\tau, \omega)$ being the integral kernel for a fermionic particle and $\mathcal{G}(\tau) = -\langle T \hat{c}_x(\tau) \hat{c}_x^\dagger \rangle$ is the single particle Green function in euclidean space-time for a fermionic excitation with quantum numbers x .¹ As $\mathcal{K}(\tau, \omega)$ vanishes exponentially for large $|\omega|$,

$$\lim_{\omega \rightarrow \pm\infty} \mathcal{K}(\omega) \rightarrow 0, \quad (2)$$

the inverse of the kernel diverges exponentially in the high frequency limit, rendering the inverse problem exponentially unstable.

In this work, we will construct a convolutional neural network to learn the analytic continuation of imaginary time Green's functions to the real frequency domain. Several other wide-spread approaches to this problem exist so far. Two common approaches are the usage of the MaxEnt algorithm [7, 8] or stochastic analytical continuation [9–11]. Both approaches are based on a χ^2 -quality of the analytic continuation as evaluated by

$$\chi^2[A] = \int d\tau d\tau' \left(\int d\omega \mathcal{K}(\tau, \omega) \hat{A}(\omega) - \mathcal{G}(\tau) \right) C^{-1}(\tau, \tau') \left(\int d\omega \mathcal{K}(\tau', \omega) \hat{A}(\omega) - \mathcal{G}(\tau') \right), \quad (3)$$

where $C(\tau, \tau')$ corresponds to the covariance matrix that accounts for correlation in imaginary time in the data. Within a stochastic evaluation of the imaginary time Green function, the Green function is given by $\mathcal{G}(\tau) = \sum_n P(n) G_n(\tau) \simeq \frac{1}{N_{\text{Samples}}} \sum_{m=1}^{N_{\text{Samples}}} G_m(\tau)$, where n denotes an arbitrary configuration space with a probability distribution $P(n)$ and N_{Samples} corresponds to the number of independent configurations, m , drawn from this probability distribution. In this context, the covariance matrix is given by [12]

$$C(\tau, \tau') = \frac{1}{N_{\text{Samples}}} \sum_{m=1}^{N_{\text{Samples}}} [G_m(\tau) - \mathcal{G}(\tau)][G_m(\tau') - \mathcal{G}(\tau')] \quad (4)$$

¹For Bose statistics the distribution changes such that $\mathcal{G}(\tau) = - \int d\omega \frac{e^{-\omega\tau}}{1 - e^{-\frac{\hbar\omega}{k_B T}}} A(\omega)$.

In the absence of correlations in imaginary time, the covariance matrix is diagonal and reduces to the square of the stochastic error.

MaxEnt involves a relative entropy functional given by

$$\mathcal{S}[A] = - \int d\omega \hat{A}(\omega) \ln \left(\frac{\hat{A}(\omega)}{D(\omega)} \right), \quad (5)$$

with $D(\omega)$ the so-called default model encoding any priori knowledge about the spectral density $\hat{A}(\omega)$ [7, 8]. MaxEnt then minimizes the combination

$$Q = \chi^2 - \alpha^{-1} \mathcal{S}, \quad (6)$$

with α^{-1} being a hyperparameter that is determined by the algorithm. In this work, we will use the so called classic implementation of MaxEnt [7, 8]. While this procedure allows for good control of the output, it has difficulty resolving high energy structures and detailed features of the spectral function. Many alternatives to the MaxEnt method have been proposed, including a stochastic approach [9–11] as well as methods based on Nevanlinna’s theorem [13]. The very difficulty of this problem calls for alternatives that can be used for comparison, and further implementations using machine learning algorithms [14, 15], including neural networks [16–19], can yield some advantages [14, 16], in particular in noise handling.

In general, trained in a supervised manner, neural network approaches are well suited to tackle this kind of ill-posed problems [6]. However, approaches differ in their structure in using dense layers only [19], using convolution layers [17, 18], or applying Softmax as a method for normalization [16]. Differently from [19], we use convolutional layers. While [17, 18] also use convolutional layers, in their approach, the convolution is applied subsequent to the dense layers, breaking the locality and translation invariance of the underlying data.

This paper is organized as follows: In sec. 2, the technical details of our implementation, as well as the generation of training and test data, and the process of training are explained. Subsequently, in sec. 3, the results of the trained network are compared to MaxEnt. In sec. 3.1, we will examine the behavior of the network and its decision making process. In particular, our network is used to detect spin-charge separation in a 1D Hubbard model in sec. 3.2 [20, 21], and applied to the two-dimension Su-Schrieffer-Heeger model on a square lattice [22, 23] in sec. 3.3. We end with a conclusion and outlook in sec. 4.

2 Computational aspects

A neural network, i.e. a network of repeating units called neurons, can be seen as a universal function approximator [24]

$$f : \mathbb{R}^n \rightarrow \mathbb{R}^m, \quad (7)$$

where $n, m \in \mathbb{N}$ describe the dimension of the input and output vector, respectively. The propagation of an input vector $\mathbf{x} \in \mathbb{R}^n$ can be described as

$$\mathbf{a} = \phi(\mathbf{W} \cdot \mathbf{x} + \mathbf{b}), \quad (8)$$

where \mathbf{a} describes the activation in the layer, \mathbf{x} the activation of the previous layer, \mathbf{W} the weight matrix, ϕ a non-linear activation function, and \mathbf{b} the bias. \mathbf{W} and \mathbf{b} are the free parameters of the model, which are adjusted while training. For training these networks in a supervised manner, a data set \mathcal{D} of N samples,

$$\mathcal{D} = \{(\mathbf{x}_0, \mathbf{y}_0), (\mathbf{x}_1, \mathbf{y}_1), \dots, (\mathbf{x}_N, \mathbf{y}_N)\}, \quad (9)$$

is used, with $\mathbf{y} \in \mathbb{R}^M$ being the output for their corresponding input vectors $\mathbf{x} \in \mathbb{R}^N$. The prediction of the network $\hat{\mathbf{y}}$ is interpreted as a function of its free parameters such that $\hat{\mathbf{y}}(\mathbf{w})$, where \mathbf{w} collectively denotes the bias \mathbf{b} and the weight matrix \mathbf{W} . While training, the problem specific loss $\mathcal{L}(\mathbf{y}, \hat{\mathbf{y}})$ is minimized using an optimization algorithm on the free parameters \mathbf{w} . Examples of commonly used optimization algorithms are stochastic gradient descent [25] or Adam [26], with the previous one being employed in our work.

2.1 Generating the training data

In the following we want to train a neural network to invert eqn. (1) which, as stated in the introduction, is an exponentially unstable problem. For supervised training of our network, a dataset of the form of eqn. (9) and size N is used,

$$\mathcal{D} = \{(\mathcal{G}_0, A(\omega)_0), (\mathcal{G}_1, A(\omega)_1), \dots, (\mathcal{G}_N, A(\omega)_N)\}, \quad (10)$$

where \mathcal{G}_i and $A(\omega)_i$ denote, respectively, the imaginary time domain Greens function and the spectral density function.

Fortunately, even though the inversion of eqn. (1) is ill-posed, eqn. (1) itself can be straightforwardly evaluated. Following [14], we generate our dataset by randomly generating spectral density functions $A(\omega)_i$ and subsequently applying eqn. (1) to calculate \mathcal{G}_i . More specifically, we construct the spectral density functions from a set of Gaussians. In [14], those Gaussian distributions were chosen to be uniformly distributed in the region of interest. In contrast, we artificially increase the overlap between these Gaussian distributions by introducing collision centers. For each sample, we randomly generate $n_{\text{col}} = 4, 5, \dots, 8$ collision centers, distributed uniformly within the frequency window $\omega_c \in [-7.5, 7.5]$. To each collision center we randomly assign $n_{\text{Gauss}} = 1, 2, \dots, 12$ Gaussian distributions. These Gaussian distributions with uniform randomly chosen variance $\sigma_{\text{Gauss}} \in [0.1, 3.0]$ are centered at the collision centers with a variance of $\sigma_{\text{col}} = 0.01$. To each Gaussian peak with variance σ_{Gauss} we assign a height h randomly drawn from a Gaussian distribution with mean

$$\bar{h} = \frac{5}{\sigma_{\text{Gauss}}^3}, \quad (11)$$

and variance $\sigma_h = 0.1$. This choice of \bar{h} is motivated by our experience of how realistic data should look like and should be generated. Moreover, we cut off the height such that $h \in [0, 100]$. Note that this is not the final height of the Gaussian in the spectral density function but, as explained below, the height prior to imposing the sum rule normalization. The final height is later rescaled to satisfy the normalization constraint, i.e. the sum rule eqn. (13).

To add non-Gaussian aspects to the training data, we randomly add $n_{\text{step}} = 1, 2, 3$ step functions to 20% of the generated data. The position of the step is uniform randomly distributed with $\omega_{\text{step}} \in [-10, 10]$. Its height is randomly drawn from a uniform distribution with $h_{\text{step}} \in [-5, 5]$. Finally, to reduce the sharpness of the step functions, we low-pass filter the training data with an Infinite Impulse Response (IIR) filter

$$\hat{\omega}(\tau_i) = (1 - \gamma)\omega(\tau_i) + \gamma\hat{\omega}(\tau_{i-1}) \quad (12)$$

where we randomly start with the smallest or the largest τ . The final height is defined by rescaling the entire spectral density function to ensure the sum rule

$$\int_{-\infty}^{\infty} A(\omega)d\omega = 1. \quad (13)$$

As the original distribution of the physical spectral density functions is unknown, we utilize this multi-step process such that the created dataset includes as many semi-realistic spectral density functions as possible. We create $N_{\text{train}} = 35008$ training and $N_{\text{test}} = 3200$ test data for inverse Monte Carlo sampling temperatures $\beta = \frac{1}{k_B T} \in \{10, 20\}$ each. For the final training, we add spatial correlated, i.e. non-white, noise [27] to the data to better mimic the noise output of the Monte-Carlo simulations. For this noise, we randomly select an inverse power-law with exponent $\alpha \in [1, 5]$.

2.2 Description of the training setup

We now turn to the description of the structure of our neural network, as well as the training procedure used.

2.2.1 Structure of the neural network

We use a Convolutional Neural Network (CNN) for predicting the spectral density function. CNNs usually consist of one or multiple convolutional layers [28] followed by a dense part. In the context of image recognition, convolutional layers are used as feature finding layers. However, in a more physics driven approach, these layers apply local operators where the locality is controlled by the size of the kernel, and enforce a translation invariance of the trained features.

As the input data are artificially made noisy and we want to invert an integral operator, the slopes of the input data, i.e. the first derivatives, are important features in the input Greens functions \mathcal{G} . As the operation of determining a slope is local and translation invariant we start our network with a set of three convolution layers calculating the slopes. As those operations do not require a bias, we only allow for adjusting the convolution weights while enforcing a zero bias. Moreover, we chose as activation functions for those layers

$$\text{PRELU}(x) = \begin{cases} x & \text{if } x \geq 0 \\ \gamma \cdot x & \text{else} \end{cases}, \quad (14)$$

with $\gamma \in \mathbb{R}$ being a trainable parameter. The convolution part of the neural network can be seen in Fig. 1 (a).

For our neural network simulations, the size of the input data, i.e. the dimensionality of the input data vector is chosen to be $n = 101$. The dense part of the CNN consists of three layers with 6336 nodes in the input, 7000 nodes in the hidden, and 7500 nodes in the output layer of the dense part. As activation function, we utilize Rectified Linear Unit (ReLU) activation functions [29], defined as

$$\text{ReLU}(x) = \begin{cases} x & \text{if } x \geq 0 \\ 0 & \text{else} \end{cases}, \quad (15)$$

The dense part of the network is depicted schematically in Fig. 1 (b).

Next, we apply a deconvolution, increasing the spatial size to 20,000 output neurons. Here, we utilize a set of two convolution transposed [30] layers as well as a final convolution layer to reduce memory requirements. As before in the convolution, we suppress the bias \mathbf{b} and only adjust the weights \mathbf{W} . However, similar to the dense part of the neural network, we use ReLU activation functions in the deconvolution part of the network. The deconvolution part of the network is depicted in Fig. 1 (c).

Finally, we apply a rescaling layer ensuring the normalization (sum rule (13)) of the output. To this end, the layer calculates the absolute area under the given spectral density function and rescales the result accordingly.

2.2.2 Loss function and trainer

To train our network, we utilize a two-fold loss function consisting of a sum of squared errors and a sum of absolute errors². The sum of squared errors is given by

$$\mathcal{L}_{12} = \sum_{i=0}^N \sum_{\omega} (A_i(\omega) - \hat{A}_i(\omega))^2, \quad (16)$$

with N being the batch size, i.e. the number of training data in a single batch. The sum of absolute errors part is given by

$$\mathcal{L}_{11} = \sum_{i=0}^N \sum_{\omega} |A_i(\omega) - \hat{A}_i(\omega)|. \quad (17)$$

²Both contributions are similar to mean squared error and mean absolute error, respectively, up to a rescaling by the batch size N .

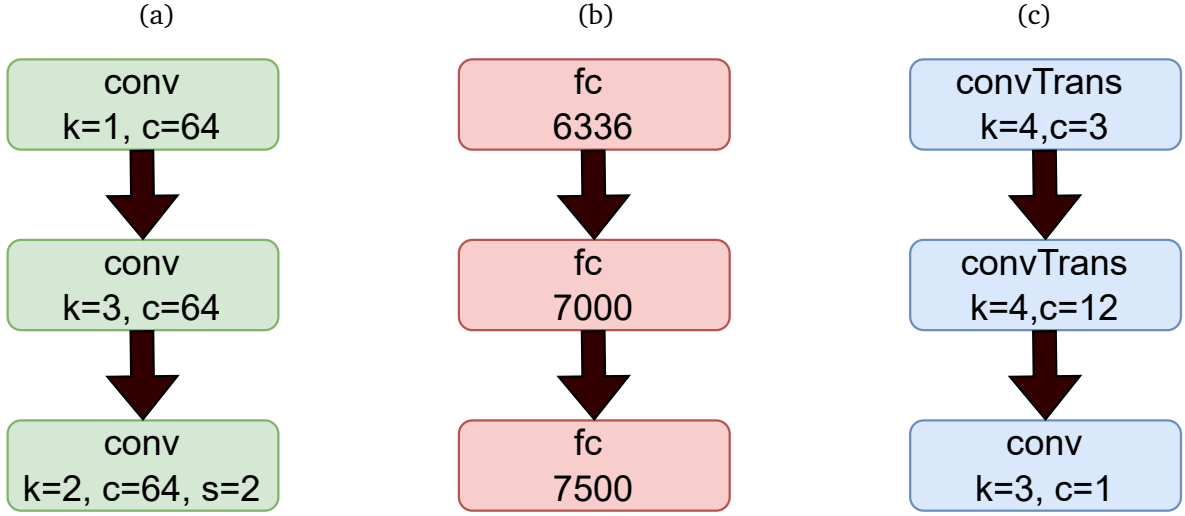


Figure 1: Scheme of the layers in the convolution (a), the dense (b), and deconvolution (c) parts of the neural networks. In (a), the top row denotes the layer type, the first value k describes the kernel size, the second value c the output channel size for this layer, and the optional third value s the stride if different to one. A similar notation applies to (c), where convolutional transposed layers are utilized. For the dense part described in (b) the corresponding layer sizes are shown.

For large deviations ($A_i(\omega) - \hat{A}_i(\omega)$) the loss is dominated by the squared error, while for smaller deviations, the loss is dominated by the absolute error. We utilize this combination as the training data consists of peaks with varying height. While larger peaks, in general, are more important to be precise, the error should not be dominated by those larger peaks, causing the network to focus mainly on those large peaks. The final loss function is given as

$$\mathcal{L} = \mathcal{L}_{12} + \mathcal{L}_{11}. \quad (18)$$

Finally, we train the neural network for 2,000 epochs with stochastic gradient descend (SGD) as optimizer, with learning rates decreasing from 10^{-2} to 10^{-5} until the networks loss saturates.

3 Performance & physical results

In the following section, the results of our neural network are compared to MaxEnt. In a first step we compare the performance of both approaches on an artificially generated validation set. Subsequently, we apply the network to two physical systems, the one-dimensional Hubbard model and the two-dimensional Su-Schrieffer-Heger (SSH) model, and discuss the performance of both approaches in recognizing the physically relevant features in those systems.

3.1 Comparison to MaxEnt on validation data

As a first test of our network, we compare its performance against MaxEnt on validation data. For this purpose, we generate additional 64 samples of data, which were neither used to train nor to test the network's performance while development. For this data set, the Greens function is calculated from an existing spectral density function, and the predictions of MaxEnt and the network are compared to the known ground truth, i.e. the analytically known result in the real frequency domain. As metrics we apply the mean square error (MSE), the mean absolut error (MAE), and the Wasserstein distance [31]. The MSE is defined as

$$\text{MSE} = \frac{1}{N} \mathcal{L}_{12}, \quad (19)$$

Metric	Network	MaxEnt
MSE ↓	0.108	0.121
MAE ↓	0.896	0.950
Wasserstein distance ↓	0.511	0.559

Table 1: Comparison of predictions by the neural network and MaxEnt to a ground truth based on a set of 64 randomly generated spectral density functions. While both algorithms perform qualitatively similar, the network consistently has a slight advantage over all metrics when applied to generated spectral functions similar to the training data. The arrow ↓ next to the name of each metric indicates that smaller values mean better performance.

where $N = 64$ and \mathcal{L}_{12} is given in eqn. 16. Similarly, the mean absolute error (MAE) is given by

$$\text{MAE} = \frac{1}{N} \mathcal{L}_{11}, \quad (20)$$

where \mathcal{L}_{11} is given in eqn. 16. Note that our neural network was trained to minimize MSE and MAE as they are given (up to scaling) by the respective loss functions (16) and (17).

Finally, in order to have another independent distance measure not built into the loss function, we employ the Wasserstein distance [31] as an independent metric, defined by

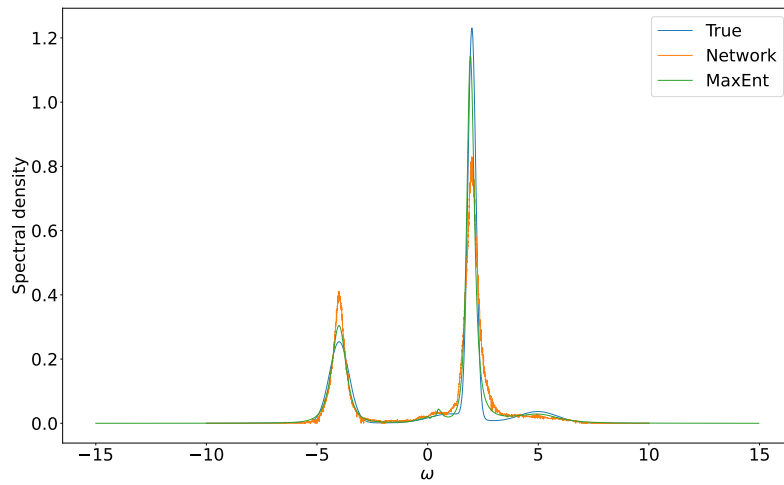
$$W_1(A, \hat{A}) = \inf_{\pi \in \Gamma(A, \hat{A})} \int_{\mathbb{R} \times \mathbb{R}} |\omega - \hat{\omega}| d\pi(\omega, \hat{\omega}), \quad (21)$$

where $\Gamma(A, \hat{A})$ is the set of all couplings (joint distributions) with marginals A and \hat{A} . Moreover, we write for $A_i(\omega)$, $\hat{A}_i(\omega)$ the short-hand notation A , \hat{A} , respectively³. Naively speaking, the Wasserstein distance quantifies the minimal transport cost, given by how large $|\omega - \hat{\omega}|$ needs to be to transform \hat{A} into A .

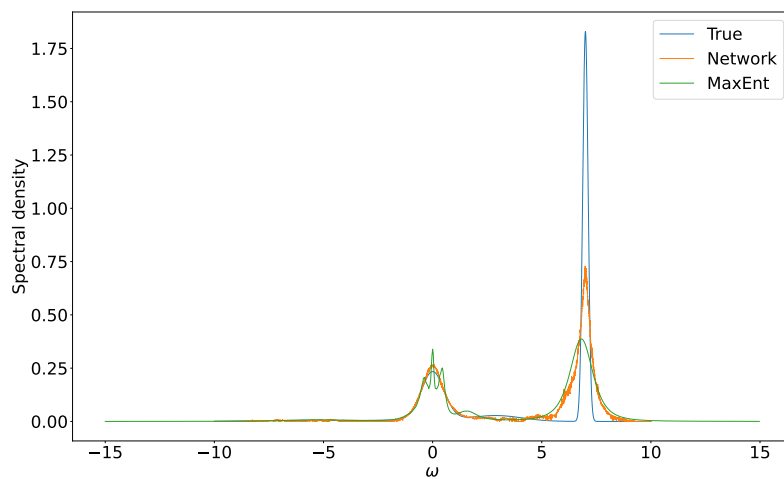
The results of this test are shown in Table 1. As can be seen, the network and MaxEnt perform roughly similar when reconstructing the spectral density function, with a slight but consistent advantage for the network on all metrics. Please note that the spectral density functions used for this comparison are generated similarly to the training and test data of the neural network and thus perfectly fit into the distribution of functions the network is trained for.

In Fig. 2, three exemplary predictions of our artificially generated data are shown. For each example, the expected spectral density function labeled 'True', as well as predictions by MaxEnt and the neural network, are provided. Here, the systematic differences between the predictions by MaxEnt and the neural network become evident. In general, our network seems to be better than MaxEnt at predicting the exact location of a high peak as can be seen in Fig. 2a and Fig. 2b on the right peak, as well as in Fig. 2c. However, MaxEnt proves to be more sensitive to small peaks, which our network sometimes ignores, c.f. e.g. in Fig. 2a the shallow 'hill' next to the highest peak and the small but steep peak in the left of Fig. 2b. The reason for this bias is the loss function described in Eq. 18. As the loss function compares the difference in height of the predicted and actual spectral density function for each ω , the loss prioritizes the exact location over the exact height, especially for sharp peaks. This raises the question whether a loss function considering spatial relations in ω such as the Wasserstein distance might be better suited for the training of the neural network. Another noteworthy aspect is the different pattern of overfitting in our neural network, as compared to MaxEnt. While the network tends to ignore smaller peaks, MaxEnt overfits aspects of the images as can be seen in Fig. 2b in the smaller peak on the left, where MaxEnt also produces oscillations, and similarly for the large peak on the left in Fig. 2c.

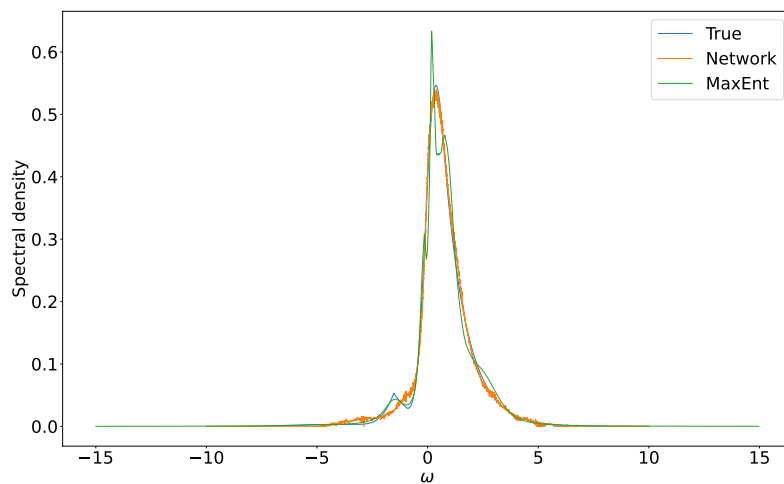
³Also see https://docs.scipy.org/doc/scipy/reference/generated/scipy.stats.wasserstein_distance.html.



(a)



(b)



(c)

Figure 2: Exemplary predictions for artificially generated data. Each example includes the true (generated) spectral density function as well as predictions by MaxEnt and the neural network. Systematic differences between the predictions of MaxEnt and the neural network can be seen in the prediction of heights and positions of peaks, as well as MaxEnt inducing oscillations around sharp peaks.

3.2 Spin-Charge separation in 1D Hubbard model

In one spatial dimension, the Fermi liquid is unstable to interactions. The electron with spin 1/2 and unit electric charge fractionalizes into two entities, the chargeless spinon carrying the spin 1/2 degree of freedom, and the spinless holon carrying the charge [32]. Importantly both entities have different velocities, and the spectral function of the electron is a convolution of the spinon and holon spectral functions. This fractionalization of the physical electron is best seen in dynamical correlation functions, for which analytical continuation is often feasible. Beyond the well-established phenomenon of spin-charge separation in one-dimensional (1D) Mott insulators, first understood via the exact Bethe ansatz solution of the Hubbard model [33], recent theoretical and experimental work has revealed the possibility of spin-orbital separation, wherein an injected electron can decay into three independently propagating quasiparticles: a spinon (carrying spin), an orbiton (carrying orbital excitation), and a holon (carrying charge). Using a microscopic model for the quasi-1D compound Sr_2CuO_3 , [34] demonstrated theoretically that spin and orbital degrees of freedom dynamically decouple. This prediction was subsequently confirmed experimentally in [35] using resonant inelastic x-ray scattering, revealing clear evidence for the independent propagation of spinons and orbitons.

The Hubbard model that we consider here does not take into account orbital degrees of freedom. Its Hamiltonian reads

$$\hat{H} = -t \sum_{i,\sigma} \left(\hat{c}_{i,\sigma}^\dagger \hat{c}_{i+1,\sigma} + \hat{c}_{i+1,\sigma}^\dagger \hat{c}_{i,\sigma} \right) + \frac{U}{2} \sum_i (\hat{n}_i - 1)^2. \quad (22)$$

Here, i labels the sites of a one-dimensional chain, $\hat{c}_{i,\sigma}^\dagger$ creates an electron with z-component of spin $\sigma = \uparrow, \downarrow$ in a Wannier state centered around site i , and $\hat{n}_i = \sum_{\sigma} \hat{c}_{i,\sigma}^\dagger \hat{c}_{i,\sigma}$ is the number operator. We carry out calculations on an $L = 46$ site chain, at $U/t = 4$ and $\beta t = 10$, with β being the inverse temperature. At vanishing chemical potential, particle-hole symmetry ensures half-filling, $\frac{1}{L} \sum_{i=1}^L \langle \hat{n}_i \rangle = 1$. We have carried out the calculations with the Algorithms for Lattice fermions (ALF) package [12] for the finite temperature auxiliary field quantum Monte Carlo algorithm [36, 37].

The key feature of the data presented in Fig. 3(b) is a gap at wave vector $k = \pi/2$. As mentioned above, a doped hole at negative energies splits into a spinon and a holon. In the simplest possible understanding, the spectral function of the electron is given by a convolution of that of the spinon and of the holon. As such, the spectral function is characterized by the absence of poles and structure distribution of the spectral weight. In particular, at $k < \pi/2$ we observe two branch cuts corresponding to the fractionalized excitations. It is challenging to resolve them as a function of k . At $k = 0$ we clearly observe two features at $\omega \simeq -1.6$ and $\omega \simeq -3.0$ corresponding to the spinon and holon, respectively. Both excitations are expected to merge together at $k = \pi/2$. Other features in the spectral function have been discussed intensively in the literature and it is beyond the scope of this article to account for the details of the physics. We refer the interested reader to Ref. [21] for more information.

In this work, we use data for the spectral function of the 1D Hubbard model obtained using the ALF package [12] to benchmark our neural network analytic continuation against the established MaxEnt method. Fig. 3(a) plots the neural network analytic continuation results. In comparison to MaxEnt we observe a loss of spectral weight at positive (negative) frequencies and negative (positive) momenta, corresponding to the so called shadow bands [38]. The Hubbard model at half-filling has dominant anti-ferromagnetic correlations such that a mode at a wave vector k can scatter off a gapless spin-excitation carrying momentum $q = \pi$, and hence generate a shadow at momentum $k + \pi$. Finally, we observe stratification of the image produced by the network, which introduces additional spurious features.

3.3 The two-dimensional SSH model: self-consistent Born approximation

As a second benchmark case, we consider a specific version of the two-dimensional Su-Schrieffer-Heeger (SSH) model [22], given by

$$\hat{H} = \sum_{b=\langle i,j \rangle} (-t + g \hat{X}_b) \left(\sum_{\sigma} \hat{c}_{i,\sigma}^\dagger \hat{c}_{j,\sigma} + \hat{c}_{j,\sigma}^\dagger \hat{c}_{i,\sigma} \right) + \sum_b \frac{\hat{p}_b^2}{2m} + \frac{k}{2} \hat{X}_b^2. \quad (23)$$

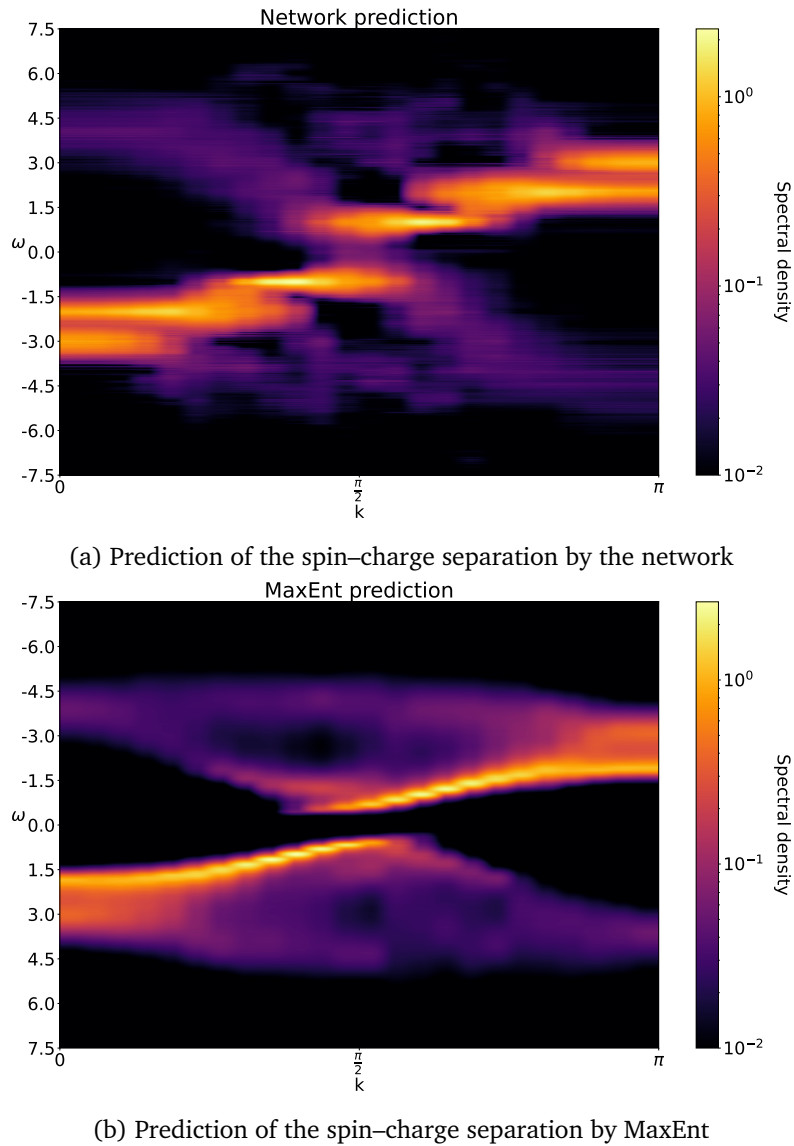
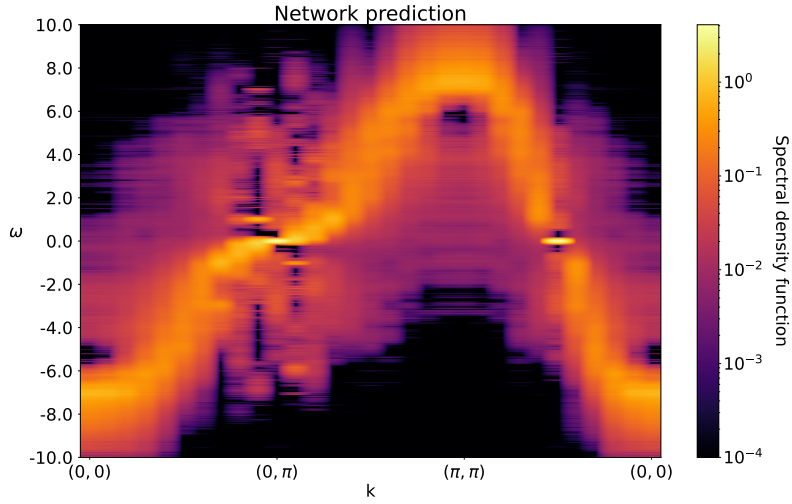


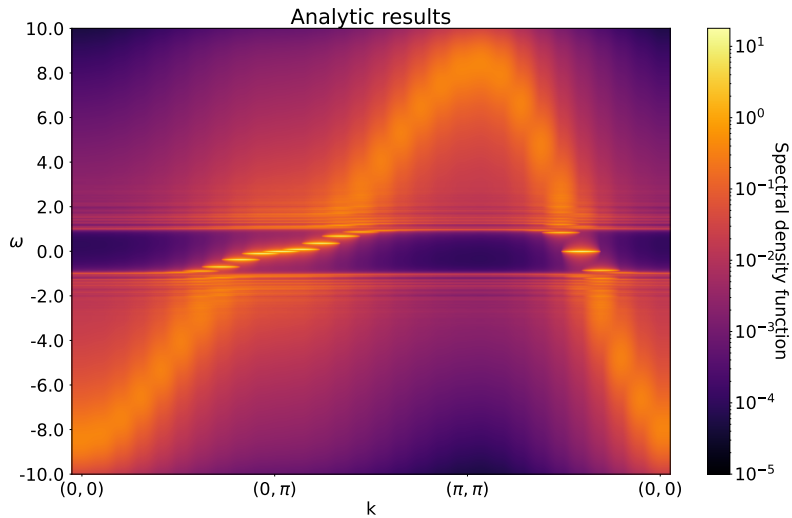
Figure 3: Predicted spectral density functions for the 1D Hubbard model using the neural network 3a and MaxEnt 3b. Here we consider an $L = 46$ site chain at $U/t = 4$ and $\frac{t}{k_b T} = 10$ at half filling. The MaxEnt plot is taken from [12]. While in both images spin-charge separation is discernible, the network produces spurious stratification of the image.

On each nearest neighbor bond b of a square lattice with sites labelled by the i, j sits a harmonic oscillator that dynamically modulates the hopping matrix element. While it is possible to carry out Monte Carlo simulations of this model [23, 39], we adopt a self-consistent Born approximation described in Ref. [23, 40]. Importantly, this approximation goes a good way at capturing some salient features of the single particle spectral function. It also allows for a calculation on the real time axis, such that no analytical continuation is required. For comparison with the neural network analytical continuation we transform the real frequency data to imaginary time – this transformation is numerically stable – and then use the neural network to transform back to real frequencies.

The data presented in Fig. 4b is taken from [23] and corresponds to the half-filling case at $\omega_0 = \sqrt{\frac{k}{m}} = 1.0$, $k_b T = 1/40$, $t = 1.85$ and $g = 1.5$. As apparent, below the phonon frequency, $|\omega| < \omega_0$, we observe a well-defined renormalized quasi-particle excitation. Above ω_0 , the coupling to the phonon degrees of freedom provide a substantial broadening of the bare dispersion relation, resulting in a substantial incoherent



(a) Prediction for the 2D SSH model by the network.



(b) Analytic results for the 2D SSH model.

Figure 4: Fig. 4a shows the neural network prediction for the spectral density of the 2D SSH model. Fig. 4b is reproduced from Fig. 12(a) of [23]. The data presented here [23] corresponds to the half-filling case at $\omega_0 = \sqrt{\frac{k}{m}} = 1.0$, $k_b T = 1/40$, $t = 1.85$ and $g = 1.5$. \mathbf{k} runs over a path in the Brillouin zone, from $(0, 0)$ to $(0, \pi)$ to (π, π) and back to $(0, 0)$. The frequency ranges from -10 to 10 in steps of 0.01 .

background. The data provides an interesting test case where coherent and incoherent excitations are to be resolved simultaneously. Upon comparison, we observe that the neural network can resolve the incoherent high energy features of the image as well as, to some degree, the low energy coherent quasi-particle excitations inside the gap, but fails to properly resolve the infrared gap itself. This is, however, not surprising, as our network is trained with data built from Gaussians, and not with data that explicitly included gaps, the latter of which hence are out of distribution samples.

4 Conclusion and Outlook

In this work, we employed a neural network to predict a spectral density function from a given imaginary-time Green's function. Training a network for this task poses several challenges, primarily due to the ill-posed nature of analytical continuation and the presence of noise in imaginary-time Green's functions. One of the central obstacles for applying machine learning to such problems is the construction of suitable training data. Due to the large variability of possible spectral density functions, we developed a multi-stage procedure for the automatic generation of artificial spectral densities.

In more detail, we proposed methods for generating high-quality training and testing data with sufficient complexity. The training data predominantly consist of Gaussian peaks. To increase the probability of peak overlap, these peaks were generated around predefined collision centers, with peak positions drawn from a normal distribution centered at each collision point. To incorporate non-smooth and unsteady features, we randomly added Heaviside step functions with both positive and negative amplitudes. In addition, a subset of the data was randomly low-pass filtered to introduce further complexity and heterogeneity. This procedure yields a rich and diverse set of spectral density functions for training the network. Furthermore, we added artificial pink noise to the data in order to closely mimic the correlated noise arising from Monte Carlo simulations of Green's functions.

We evaluated the performance of the neural network by comparing it to MaxEnt, as well as by applying it to established physical models, including spin-charge separation in the one-dimensional Hubbard model, as well as the SSH model on a square lattice within the self-consistent Born approximation. Using an additional set of artificially generated validation data, we found that the chosen loss function enforces a stricter localization of peak maxima, while being less accurate in predicting peak heights than MaxEnt. Nevertheless, on this validation data, the network outperforms MaxEnt across all tested metrics, including the mean squared error and the Wasserstein distance. This highlights the potential of neural network based approaches for addressing ill-posed inverse problems. For physically motivated tests, most notably spin-charge separation in the one-dimensional Hubbard model studied using auxiliary-field quantum Monte Carlo methods [12], as well as the electron-phonon problem treated within the self-consistent Born approximation [23], the network currently performs worse than MaxEnt.

We therefore conclude that, while the artificial training data partially capture relevant physical features, insufficient coverage remains a limiting factor for network performance. This discrepancy indicates a systematic difference between artificial and real data that has yet to be resolved within the data generation process. Despite these limitations, the results suggest that further improvements in the training data generation scheme could enhance the network's capabilities beyond those of MaxEnt. At present, the dominant limitation arises from the data generation procedure and the presence of out-of-distribution samples when applying the network to physical data.

In practice, the network provides an easy-to-use tool that already yields reasonably accurate identification of physically relevant features. More broadly, our results demonstrate that neural networks are, in principle, capable of solving this task and point toward future research directions with the goal to further improve the network's capabilities. Beyond artificial data generation, the network could also be trained on experimental spectroscopic data available online and in established databases. Real-frequency spectral data, once digitized, can be transformed into imaginary-time data in the stable direction of the problem. The resulting paired data sets of imaginary- and real-frequency information can then be used directly for training. Experimental data

may further be complemented by results from various approximation methods such as the self-consistent Born approximation discussed in this work to further enrich the training set. In summary, this raises an important question of how much data are required to train a neural network that consistently outperforms standard analytical continuation methods?

Acknowledgements

We thank Robert Helling for useful discussions.

Author contributions The core methodology and neural network framework were developed and implemented by Martin Rackl and Yanick Thurn. Data for testing and Maximum Entropy analysis were contributed by Fakhre Assaad and Anika Götz. Johanna Erdmenger and René Meyer contributed through scientific consultation and conceptual guidance. All authors contributed to the writing of the manuscript.

Funding information The authors acknowledge financial support by the Deutsche Forschungsgemeinschaft (DFG, German Research Foundation) through the Würzburg-Dresden Cluster of Excellence ctd.qmat – Complexity, Topology and Dynamics in Quantum Matter (EXC 2147, project-id 390858490), and through the Collaborative Research centre “ToCoTronics”, Project-ID 258499086-SFB 1170. We also acknowledge financial support by the DFG through the German-Israeli ProjectCooperation (DIP) grant ‘Holography and the Swampland’.

References

- [1] G. Policastro, D. T. Son and A. O. Starinets, *Shear viscosity of strongly coupled $n=4$ supersymmetric yang-mills plasma*, Physical Review Letters **87** (2001).
- [2] P. K. Kovtun, D. T. Son and A. O. Starinets, *Viscosity in strongly interacting quantum field theories from black hole physics*, Physical review letters **94** (2005).
- [3] D. A. Teaney, *Viscous hydrodynamics and the quark gluon plasma*, In *Quark-Gluon Plasma 4*, pp. 207–266. World Scientific (2010).
- [4] J. W. Negele and H. Orland, *Quantum Many-particle Systems*, Westview Press, ISBN 0738200522 (1998).
- [5] S. Sachdev, *The landscape of the Hubbard model*, In *Theoretical Advanced Study Institute in Elementary Particle Physics: String theory and its Applications: From meV to the Planck Scale*, pp. 559–620, doi:10.1142/9789814350525_0009 (2010), 1012.0299.
- [6] A. Tanaka, A. Tomiya and K. Hashimoto, *Deep Learning and Physics*, Springer Nature, Singapore (2021).
- [7] M. Jarrell and J. Gubernatis, *Bayesian inference and the analytic continuation of imaginary-time quantum monte carlo data*, Physics Reports **269**(3), 133 (1996), doi:https://doi.org/10.1016/0370-1573(95)00074-7.
- [8] W. von der Linden, *Maximum-entropy data analysis*, Applied Physics A **60**(2), 155 (1995), doi:10.1007/BF01538241.
- [9] K. S. D. Beach, *Identifying the maximum entropy method as a special limit of stochastic analytic continuation*, arXiv e-prints cond-mat/0403055 (2004), doi:10.48550/arXiv.cond-mat/0403055, cond-mat/0403055.

- [10] A. Sandvik, *Stochastic method for analytic continuation of quantum monte carlo data*, Phys. Rev. B **57**, 10287 (1998), doi:10.1103/PhysRevB.57.10287.
- [11] H. Shao and A. W. Sandvik, *Progress on stochastic analytic continuation of quantum monte carlo data*, Physics Reports **1003**, 1 (2023), doi:https://doi.org/10.1016/j.physrep.2022.11.002, Progress on stochastic analytic continuation of quantum Monte Carlo data.
- [12] F. F. Assaad, M. Bercx, F. Goth, A. Götz, J. S. Hofmann, E. Huffman, Z. Liu, F. P. Toldin, J. S. E. Portela and J. Schwab, *The ALF (Algorithms for Lattice Fermions) project release 2.4. Documentation for the auxiliary-field quantum Monte Carlo code*, SciPost Phys. Codebases pp. 1–v2.4 (2025), doi:10.21468/SciPostPhysCodeb.1-v2.4.
- [13] J. Fei, C.-N. Yeh and E. Gull, *Nevanlinna analytical continuation*, Phys. Rev. Lett. **126**, 056402 (2021), doi:10.1103/PhysRevLett.126.056402.
- [14] L.-F. Arsenault, R. Neuberg, L. A. Hannah and A. J. Millis, *Projected regression methods for inverting fredholm integrals: Formalism and application to analytical continuation* (2016), 1612.04895.
- [15] I. S. Krivenko and A. N. Rubtsov, *Analytic continuation of quantum monte carlo data: Optimal stochastic regularization approach* (2006), cond-mat/0612233.
- [16] R. Fournier, L. Wang, O. V. Yazyev and Q. Wu, *Artificial neural network approach to the analytic continuation problem*, Phys. Rev. Lett. **124**, 056401 (2020), doi:10.1103/PhysRevLett.124.056401.
- [17] H. Yoon, J.-H. Sim and M. J. Han, *Analytic continuation via domain knowledge free machine learning*, Phys. Rev. B **98**, 245101 (2018), doi:10.1103/PhysRevB.98.245101.
- [18] K.-W. Sun and F. Wang, *Neural network analytic continuation for monte carlo: Improvement by statistical errors*, Chinese Physics B **32**(7), 070705 (2023), doi:10.1088/1674-1056/accd4c.
- [19] J. Yao, C. Wang, Z. Yao and H. Zhai, *Noise enhanced neural networks for analytic continuation*, Machine Learning: Science and Technology **3**(2), 025010 (2022), doi:10.1088/2632-2153/ac6f44.
- [20] R. Preuss, A. Muramatsu, W. von der Linden, P. Dieterich, F. F. Assaad and W. Hanke, *Spectral properties of the one-dimensional hubbard model*, Phys. Rev. Lett. **73**, 732 (1994), doi:10.1103/PhysRevLett.73.732.
- [21] A. Abendschein and F. F. Assaad, *Temperature dependence of spectral functions for the one-dimensional hubbard model: Comparison with experiments*, Phys. Rev. B **73**, 165119 (2006), doi:10.1103/PhysRevB.73.165119.
- [22] W. P. Su, J. R. Schrieffer and A. J. Heeger, *Soliton excitations in polyacetylene*, Phys. Rev. B **22**, 2099 (1980), doi:10.1103/PhysRevB.22.2099.
- [23] A. Götz, S. Beyl, M. Hohenadler and F. F. Assaad, *Valence-bond solid to antiferromagnet transition in the two-dimensional su-schrieffer-heeger model by langevin dynamics*, Phys. Rev. B **105**, 085151 (2022), doi:10.1103/PhysRevB.105.085151.
- [24] P. Mehta, M. Bukov, C.-H. Wang, A. G. Day, C. Richardson, C. K. Fisher and D. J. Schwab, *A high-bias, low-variance introduction to machine learning for physicists*, Physics Reports **810**, 1 (2019), doi:https://doi.org/10.1016/j.physrep.2019.03.001, A high-bias, low-variance introduction to Machine Learning for physicists.
- [25] S. Ruder, *An overview of gradient descent optimization algorithms* (2016), 1609.04747.
- [26] D. P. Kingma and J. Ba, *Adam: A method for stochastic optimization* (2014), 1412.6980.

- [27] M. Morikawa and A. Nakamichi, *Solar flare $1/f$ fluctuations from amplitude-modulated five-minute oscillation*, Entropy **25**(12) (2023), doi:10.3390/e25121593.
- [28] V. Dumoulin and F. Visin, *A guide to convolution arithmetic for deep learning* (2016), 1603.07285.
- [29] K. He, X. Zhang, S. Ren and J. Sun, *Delving deep into rectifiers: Surpassing human-level performance on imagenet classification*, In *2015 IEEE International Conference on Computer Vision (ICCV)*, pp. 1026–1034, doi:10.1109/ICCV.2015.123 (2015).
- [30] M. D. Zeiler, D. Krishnan, G. W. Taylor and R. Fergus, *Deconvolutional networks*, In *2010 IEEE Computer Society Conference on Computer Vision and Pattern Recognition*, pp. 2528–2535, doi:10.1109/CVPR.2010.5539957 (2010).
- [31] M. Nakazato and S. Ito, *Geometrical aspects of entropy production in stochastic thermodynamics based on wasserstein distance*, Phys. Rev. Res. **3**, 043093 (2021), doi:10.1103/PhysRevResearch.3.043093.
- [32] T. Giamarchi, *Quantum physics in one dimension*, Clarendon Press, Oxford, ISBN 0 19 85 25 00 1 (2004).
- [33] E. H. Lieb and F. Y. Wu, *Absence of mott transition in an exact solution of the short-range, one-band model in one dimension*, Phys. Rev. Lett. **20**(25), 1445 (1968), doi:10.1103/PhysRevLett.20.1445.
- [34] J. Ritschel, S. Sykora, F. Malek, K. W. Becker and H. Fehske, *Spin-orbital separation in the quasi-one-dimensional mott insulator sr_2cuo_3* , Phys. Rev. B **73**, 165119 (2006), doi:10.1103/PhysRevB.73.165119.
- [35] J. Schlappa, K. Wohlfeld, K. J. Zhou, M. Mourigal, M. W. Haverkort, V. N. Strocov, L. Hozoi, C. Monney, S. Nishimoto, S. Singh, A. Revcolevschi, J.-S. Caux *et al.*, *Spin-orbital separation in the quasi-one-dimensional mott insulator sr_2cuo_3* , Nature **485**, 82 (2012), doi:10.1038/nature10974.
- [36] R. Blankenbecler, D. J. Scalapino and R. L. Sugar, *Monte carlo calculations of coupled boson-fermion systems.*, Phys. Rev. D **24**, 2278 (1981), doi:10.1103/PhysRevD.24.2278.
- [37] S. White, D. Scalapino, R. Sugar, E. Loh, J. Gubernatis and R. Scalettar, *Numerical study of the two-dimensional hubbard model*, Phys. Rev. B **40**, 506 (1989), doi:10.1103/PhysRevB.40.506.
- [38] K. Penc, K. Hallberg, F. Mila and H. Shiba, *Shadow band in the one-dimensional infinite- U hubbard model*, Phys. Rev. Lett. **77**, 1390 (1996), doi:10.1103/PhysRevLett.77.1390.
- [39] A. Götz, M. Hohenadler and F. F. Assaad, *Phases and exotic phase transitions of a two-dimensional su-schrieffer-heeger model*, Phys. Rev. B **109**, 195154 (2024), doi:10.1103/PhysRevB.109.195154.
- [40] F. F. Assaad, *Spin, charge, and single-particle spectral functions of the one-dimensional quarter filled holstein model*, Phys. Rev. B **78**, 155124 (2008), doi:10.1103/PhysRevB.78.155124.